X-ray Energy Spectra of the Super-soft X-ray Sources CAL87 and RXJ0925.7–4758 Observed with ASCA

Ken Ebisawa[1], Koji Mukai[1], Taro Kotani[2]

Laboratory for High Energy Astrophysics, NASA/GSFC, Greenbelt, MD, 20771, USA

Kazumi Asai, Tadayasu Dotani, Fumiaki Nagase

Institute of Space and Astronautical Science, Yoshinodai, Sagamihara, Kanagawa, 229-8510 Japan

H. W. Hartmann, J. Heise

SRON Laboratory for Space Research, Sorbonnelaan 2, NL-3584 CA Utrecht, The Netherlands

P. Kahabka[3]

Astronomical Institute and Center for High Energy Astrophysics, University of Amsterdam, Kruislaan 403, 1098 SJ Amsterdam, The Netherlands

and

A. van Teeseling

Universitäts-Sternwarte, Geismarlandstr. 11, 37083, Götteingen, Germany

ABSTRACT

We report observation results of the super-soft X-ray sources (SSS) CAL87 and RXJ0925.7–4758 with the X-ray CCD cameras (Solid-state Imaging Spectrometer; SIS) on-board the ASCA satellite. Because of the superior energy resolution of SIS ($\Delta E/E \sim 10\%$ at 1 keV) relative to previous instruments, we could study detailed X-ray spectral structure of these sources for the first time. We have applied theoretical spectral models to CAL87, and constrained the white dwarf mass and intrinsic luminosity as $0.8 - 1.2 M_{\odot}$ and 4×10^{37}–1.2×10^{38} erg s^{-1}, respectively. However, we have found the observed luminosity is an order of magnitude smaller than the theoretical estimate, which indicates the white dwarf is permanently blocked by the accretion disk, and we are observing a scattering emission by a fully ionized accretion disk corona (ADC) whose column density is $\sim 1.5 \times 10^{23}$ cm^{-2}. Through simulation, we have shown that

[1]code 662, also Universities Space Research Association

[2]code 661, also National Research Council

[3]Present address: Sternwarte, Universitaet Bonn, Auf dem Huegel 71, 53121 Bonn, Germany

the orbital eclipse can be explained by the ADC model, such that a part of the extended X-ray emission from the ADC is blocked by the companion star filling its Roche lobe.

We have found that very high surface gravity and temperature, $\sim 10^{10}$ cm s^{-2} and $\sim$100 eV respectively, as well as a strong absorption edge at $\sim$ 1.02 keV, are required to explain the X-ray energy spectrum of RXJ0925.7–4758. These values are only possible for an extremely heavy white dwarf near the Chandrasekhar limit. Although the super soft source luminosity should be $\sim 10^{38}$ erg s^{-1} at the Chandrasekhar limit, the observed luminosity of RXJ0925.7–4758 is nearly two orders of magnitude smaller even assuming an extreme distance of $\sim$ 10 kpc. To explain the luminosity discrepancy, we propose a model that very thick matter which was previously ejected from the system, as a form of jets, intervenes the line of sight, and reduces the luminosity significantly due to Thomson scattering.

Subject headings: X-rays; white dwarfs; super-soft sources; individual, CAL87 and RXJ0925.7–4758

1. Introduction

Dozens of the Super Soft X-ray Sources (SSS), which characteristically are radiating most energies in the softest X-ray energy band ($\lesssim$ 0.5 keV), have been discovered in LMC, SMC, M31 and Milky Way by *Einstein* and ROSAT (for review, e.g., Kahabka and van den Heuvel 1997). It is believed that most SSS are white dwarf binaries with large mass accretion rates ($\sim 1-5\times10^{-7}M_{\odot}$ yr^{-1}), and the energy source is steady nuclear burning on the white dwarf surface (van den Heuvel et al. 1992; Heise et al. 1994). Observationally, our knowledge on the X-ray energy spectra of SSS has been limited by the capability of the conventional X-ray detectors. While the energy bands of the *Einstein* IPC and ROSAT PSPC (0.1 – 2 keV) are suitable for the study of SSS, their energy resolutions ($\Delta E/E \gtrsim 1$ at 0.5 keV) have not allowed one to clearly identify any possible spectral structures such as emission lines or absorption edges. Having a superior energy resolution ($\Delta E/E \sim 10\%$ at 0.5 keV), the ASCA Solid State Spectrometer (SIS; Tanaka, Inoue and Holt 1994) is potentially a powerful instrument for spectroscopic study of SSS, though its detectable energy band (0.4 – 10 keV) is slightly too high to cover the typical SSS spectra.

The two SSS, CAL87 and RXJ0925.7–475, are known to have relatively hard energy spectra, thereby we have chosen these two sources for precise spectral study with the ASCA SIS. While most SSS have characteristic blackbody temperatures of $\lesssim$ 30 eV, those of CAL87 and RXJ0925.7–475 are $\gtrsim$ 40 eV (Schmidtke et al. 1993; Motch, Hasinger and Pietsch 1994). CAL87 was discovered during the LMC survey observations with the *Einstein* IPC (Long, Helfand and Grabelsky 1981). It is an eclipsing binary with a 10.6 hour orbital period, exhibiting orbital eclipses in the optical band and accompanying shallow X-ray dips (Schmidtke et al. 1993; Alcock et al. 1997; Asai et al. 1998). With the assumption that the non-degenerate companion is a F-star, Cowley et al. (1990)

speculated that the compact object is massive and may be a black hole. However, HST observations revealed two adjacent stars at 0.″88 and 0.″65 from CAL87 (Deutsch et al. 1996), which have yet to be taken into account to determine the optical properties of CAL87. Schandl, Meyer-Hofmeister and Meyer (1997) successfully modeled the observed optical light curve of CAL87 assuming a 0.75 $M_\odot$ white-dwarf and a 1.5 $M_\odot$ companion. To account for the shallow X-ray dips, the Accretion Disk Corona (ADC) model was proposed in which the blocking material partially covers the largely extended X-ray emitting corona (Schmidtke et al. 1993).

RXJ0925.7–475 was discovered in the ROSAT Galactic Plane survey project (Motch, Hasinger and Pietsch 1994). This unusual, heavily absorbed star exhibits most X-ray emission at energies above $\sim$ 0.5 keV, while most other SSS have little X-rays above $\sim$ 0.5 keV (Motch, Hasinger and Pietsch 1994; Motch 1996). The orbital period is $\sim$ 3.8 days, and the optical counterpart indicates strong reddening (Motch, Hasinger and Pietsch 1994; Motch 1996; Schmidtke et al. 2000). A transient optical jet, similar to those observed from other super-soft sources, has been also observed (Motch 1998). The reddening, strength of the interstellar absorption lines, and ROSAT spectra are all consistent with a large hydrogen column density of $N_H \gtrsim 10^{22}$ cm^{-2}, which suggests that the source is located behind the nearby (d=425 pc) Vela Sheet molecular cloud (Motch, Hasinger and Pietsch 1994). Optical light curve analysis suggests that mass of the compact object is in the range of 0.5 – 1.7 $M_\odot$ and that of the donor star is in 1 – 2 $M_\odot$ (Schmidtke et al. 2000).

In this paper, we report precise analysis of the X-ray energy spectra of CAL87 and RXJ0925.7–4758 observed with ASCA. Owing to the superior energy resolution of the ASCA SIS, we could reveal detailed X-ray spectral features of the two sources. The ASCA CAL87 light curve exhibits shallow orbital eclipses, and its energy spectrum show deep absorption edges which are identified as O VII and O VIII edges, as already reported by Asai et al. (1998). Preliminary spectral analysis of RXJ0925.7–4758 has been reported by Ebisawa et al. (1996), and similar ASCA spectral analysis has been also carried out by Shimura (2000). As an extension of these studies, we apply theoretical LTE (Local Thermal Equilibrium) and Non-LTE white-dwarf atmospheric spectral models to CAL87 and RXJ0925.7–4758, and constrain the white dwarf parameters. Also, we carry out a simulation to explain the CAL87 orbital light curve in the framework of the accretion disk corona (ADC) model, such that a part of the extended ADC X-ray emission is blocked by a companion star and observed as a shallow and wide orbital eclipse.

2. Observations

RXJ0925.7–475 was observed with ASCA from 13:28UT on December 22 1994 to 02:02UT on December 23. CAL87 was observed from 06:08UT on September 6, 1996 to 08:30UT on September 8. ASCA carries two SIS (SIS0 and SIS1) and two GIS (Gas Imaging Spectrometers; GIS2 and GIS3) detectors, each combined with an X-ray telescope, and the four sensors pointing the same direction (Tanaka, Inoue and Holt 1994). Since RXJ0925.7–475 and CAL87 do not emit significantly in the GIS energy band (0.7–10 keV), we could not detect enough photons with GIS to carry out a spectral

analysis. Therefore, we present only the SIS spectral analysis results in this paper. The GIS data of RXJ0925.7–475 was used only for a coherent pulsation search, but we obtained null results in the frequency range 2×10^{-4} to 8 Hz. After appropriate SIS data screening, the total exposure time was 15 ksec for RXJ0925.7–475 and 70 ksec for CAL87. The SIS 1CCD FAINT mode was used for both observations, and we applied the standard instrumental calibration. On each detector, the X-ray source photons were accumulated within ~ 4 arcmin from the center of the source. Having made sure that both SIS detectors gave identical results, we combined the data and responses from the two sensors for further analysis to achieve better statistics. The background spectra were made from the region on the same chips where source photons are negligible, normalized by the selected area, and subtracted from the source spectra. Spectral fitting analysis was carried out with XSPEC spectral fitting package (Arnaud 1996). For CAL87, we used essentially the same dataset as in Asai et al. (1998). Average count rates of the sources after background subtraction are 0.015 cts/s/SIS for CAL87 (orbit averaged) and 0.28 cts/s/SIS for RXJ0925.7–475, respectively, in 0.4 – 2.0 keV.

3. Data Analysis

3.1. CAL87

As reported by Asai et al. (1998), ASCA data indicates shallow ($\sim 60\%$) and wide ($\sim 30\%$ of the period) X-ray dips in phase with the optical eclipse of the white dwarf, which confirms the ROSAT results (Schmidtke et al. 1993; Kahabka, Pietsch and Hasinger 1994). In order to study spectral variation, we extracted spectra from the eclipse and out of the eclipse period in addition to the entire averaged spectrum. We took the ephemeris and orbital period from Alcock et al. (1997); the X-ray eclipse center (orbital phase ϕ=0) is MJD=50331.9103 and the period is 0.44267714 day. For the eclipse period, we took the orbital period $-0.16 < \phi < 0.16$ (see the orbital light curve, Fig. 2 in Asai et al. 1998), outside of which is considered the non-eclipse period.

We take into account both the interstellar absorption in the Milkyway and an intrinsic absorption within the LMC. In the spectral model fitting, following Asai et al. (1998), we fix the former column density at 8×10^{20} cm^{-2} and allow the latter one to be free. We assume the cosmic abundance for the Milkyway absorption, and half the metal abundance for the LMC absorption (Vassiliadis and Wood 1994; Dennefeld 1989). In the Tables below, we show only the amount of intrinsic absorption in the LMC thus determined.

3.1.1. Spectral Analysis with Blackbody + Edges

First, to characterize the observed spectrum, we analyze the energy spectrum applying a simple phenomenological model, and consider how much we can tell about the source with minimum assumptions. We use the average spectrum taken from the entire period.

As we have shown in Asai et al. (1998), the CAL87 spectral fit requires a deep absorption edge at ~ 0.85 keV, which may be interpreted due to O VII and O VIII edges at 0.74 keV and 0.87 keV respectively; these two edges are so close and the source flux is low, ASCA SIS cannot resolve them. We fit the spectrum with these absorption edges with the fixed energies. The optical depth of the O VIII edge is not constrained, so we fixed it to 10.0, which practically allow no photons to escape above the edge energy. In this model, normalization of the continuum (= effective emission area), temperature, and amount of absorption are strongly correlated, and hardly constrained (Table 1, left column).

We may constrain the temperature based on a simple physical consideration, from the fact that the O VII and O VIII edges are observed simultaneously. If we assume the LTE condition, the ionization balance is determined by the temperature, T, and the electron density, $N_{\rm e}$, through the Saha relation. The electron density can be related with the temperature and the pressure by the equation of state $n_e \approx P/kT$. Neglecting the radiation pressure, the gas pressure may be estimated from the hydrostatic equilibrium condition as $P \approx g/\kappa_{\rm R}$, where g is the surface gravity, which is typically 10^8 to 10^9 cm s^{-2} for white dwarfs, and $\kappa_{\rm R}$ is the Rosseland mean opacity, ~ 0.4 cm^2 g^{-1}. From these relations, for a typical temperature of several tens of eV, the electron densities in the white dwarf atmosphere of an optical depth of $\sim$ unity are considered to be in the range of 10^{18} to 10^{19} cm^{-3}. In Figure 1, we show the ion ratios for C, N, O, Ne and Fe calculated from the Saha relation as functions of the temperature, for the two electron densities $n_e = 10^{18}$ and 10^{19} cm^{-3}. It is seen that the condition that the O VII and O VIII edges are both present (with O VIII being more abundant) requires $T \approx 60$ – 80 eV.

Therefore we fix the blackbody temperature at 75 eV. The results are shown in Figure 2 and Table 1 (right column). We found the radius and luminosity with $T = 75$ eV are reasonable for a massive ($\gtrsim 1\ M_\odot$) white dwarf (section 4.1.1; Figure 13). Thus, based on a simple model, we see that the energy spectrum of CAL87 is likely to be explained by atmospheric emission from a massive white dwarf. Our data suggest that the energy spectrum emitted from the white-dwarf atmosphere, where the strong absorption edges are produced, is directly seen. Consequently, if the white dwarf is permanently blocked from the line-of-sight by outer part of the accretion disk (Schandl, Meyer-Hofmeister and Meyer 1997) and/or the X-rays are coming from extended ADC (Schmidtke et al. 1993), the corona has to be optically thin so that the scattering does not smear the absorption edges.

3.1.2. Theoretical White-dwarf Models

As shown in the previous section, it is likely that the energy spectrum of CAL87 is explained by emission from a hot white-dwarf atmosphere. Therefore, we next apply theoretical white-dwarf spectral models to constrain the white-dwarf parameters.

We adopt the same LTE (local thermal equilibrium) model used by Heise, van Teeseling and

Kahabka (1994) and van Teeseling, Heise and Kahabka (1996) to fit the SSS energy spectra, and the NLTE (non-LTE) model by Hartmann and Heise (1997). In both models, plane parallel geometry and hydrostatic equilibrium are assumed, and energy spectra have been calculated for given surface gravities, g, and effective temperatures, T_{eff}. In the NLTE model, the photoionization effect is additionally taken into account to calculate the ionization balance. In the LTE model, all the ions of H, He, C, N, O, Ne, Mg, Si, P, Ar, Ca, Fe and Ni are taken into account, and all the edges are included. In the NLTE model, only major ions and atomic levels of H, He, C, N, O and Ne are included (see Hartmann and Heise 1997 for detail).

Complex line opacities and line blanketing are not taken into account in both models. Significance of the line opacities as well as the non-LTE effects in the emerging spectra has been studied by several authors such as Rauch (1997), Hartmann et al. (1999) and Barman et al. (2000). The NLTE model not including the line opacities (the same model used in this paper) results in the absorption edges at higher energies compared to the LTE model with the same effective temperature, as well as a significant amount of the high-energy flux (Hartmann and Heise 1997). Additionally including the line opacity to the NLTE model reduces the edge energies and high-energy flux (Hartmann et al. 1999), but not down to the same level as the LTE model (Barman et al. 2000). Therefore, although there are systematic differences among the NLTE models by different authors, the "correct" model spectrum is expected to lie between the LTE and NLTE model spectra we use to fit the observed spectra. In that sense, we will be presenting conservative limits of the white dwarf parameters in the present paper.

To fit the observed data with these models for a given surface gravity, the best-fit temperature is searched for by interpolating one dimensional temperature grids on which model spectra have been precalculated; the temperature grids are every 5×10^4 K from 5×10^5 K to 10^6 K for the LTE model, and every 10^4 K from 3×10^5 K to 10^6 K for the NLTE model. The models mildly depend on the surface gravity, but the temperature and gravity are hardly determined simultaneously (see section 3.1.3). We adopt a surface gravity of 10^9 cm s^{-2}, which is appropriate for a massive white dwarf with a mass $\gtrsim 1 M_\odot$; validity of this assumption is checked a posteriori (section 4.1.1). The models also weakly depend on the elemental abundances. For CAL87, the LMC abundance in which metalicity is a quarter to half of the cosmic abundance is used, either taken from Vassiliadis and Wood (1994) (LTE model) or Dennefeld (1989) (NLTE model). Effects of changing the surface gravity and abundances are discussed in section 3.1.3 and 3.2.2.

In Table 2 and Figure 3, we show the results of the LTE model fit with $g = 10^9$ cm s^{-2}. The best-fit temperature, normalization (= effective emission area) and hydrogen column density have been determined for the average, eclipse, and out of the eclipse spectra. To fit the eclipse and out of the eclipse spectra, the temperature and either column density or normalization are fixed to the best-fit values determined from the average spectrum, since these parameters are not constrained simultaneously. Confidence contour map of the hydrogen column density and the effective emission area is shown in Figure 5.

The model gives acceptable fits. The temperature is tightly constrained, as expected from the condition that both O VII and O VIII are present (section 3.1.1). In addition to the O VII and O VIII edges, the best-fit model shows N VII and C VI edges (see Figure 3). Although the temperature is constrained, the normalization and the hydrogen column density are strongly correlated (Figure 5), and the effective emission area is uncertain by about a factor of two. This is because the energy band of ASCA SIS is above ~ 0.5 keV, where model spectra are not very sensitive to slight change of the column densities. Contemporary instruments having both better energy resolution and sensitivity below ~ 0.5 keV, such as the grating spectrometers on Chandra or XMM-Newton, will be able to constrain the column density and normalization simultaneously. In section 4.1.1, we will compare the observed luminosity and radius with those predicted by theoretical calculations, and discuss the white dwarf parameters. The spectral change during the eclipse is explained either due to an increase of the hydrogen column density by $\sim 5 \times 10^{20}$cm^{-2} or a decrease of the emission area by ~ 20 % (see section 4.1.2; also see Asai et al. 1998).

Results of the NLTE model ($g = 10^9$ cm s^{-2}) fit, which is equally successful, are shown in Figure 4 and Table 3. A contour map of the hydrogen column density and the effective emission area are shown in Figure 5 with that for the LTE model. Compared to the LTE model, the best-fit temperature is significantly lower; this is considered due to photoionization effects. The importance of photoionization may be roughly estimated using the ionization parameter $\xi \equiv L/nr^2$, where L, n and r are luminosity, density and radius, respectively. On the nuclear-burning white dwarf with a surface gravity of 10^9 cm s^{-2} and an effective temperature of ~ 60 eV, ξ is estimated as 1 – 10. This is large enough to ionize C, N, O and Ne to the helium-like or hydrogenic stages (e.g., Kallman and McCray 1982). Therefore, the effects of photoionization are significant, and the same ionization degree as with the LTE model is achieved at a lower temperature in the NLTE model (Hartmann and Heise 1997). Compared to the LTE model, the hydrogen column density is smaller and the best-fit surface area is twice as large in the NLTE model because of the significantly smaller temperature (Figure 5).

3.1.3. Effects of Surface Gravity and Elemental Abundances

The maximum effective temperature expected on the white dwarf surface is constrained by the Eddington luminosity, and may be expressed as $T_{eff}^{(max)} \sim 0.5\ g^{1/4}$ eV, where g is the surface gravity, which is in the range of $\sim 10^7$ – 10^{10} cm $^{-2}$ (Figure 13) and almost uniquely determined as a function of mass using a standard mass-radius relation (section 4.1.1). Correspondingly, $T_{eff}^{(max)}$ will be in the range of ~ 30 to 90 eV depending on the white dwarf mass.

To see the effect of changing the surface gravity and elemental abundances, we calculate theoretical spectral models for different surface gravities with the cosmic abundance (metal-richer than the LMC abundance), and fit the observed spectra. First, we find that the models with $g = 10^8$ cm s^{-2} cannot account for the CAL87 energy spectra, since the possible temperatures are too low to produce the observed high energy photons. Results of the fitting with $g = 10^9$ and 10^{10} cm s^{-2}

are summarized in Table 4.

The following points are noticeable from the model fitting results: (1) Models with different surface gravities can equally fit the data (unless surface gravity is too low to attain a sufficiently hot temperature). (2) For the same gravity and abundances, always the NLTE model gives a lower temperature than the LTE model, because photoionization enables to achieve the same ionization state at a lower temperature. (3) Models with higher gravities require higher temperatures. (4) An abundance change does not significantly change the results for the LTE model, but in the NLTE model a higher metal abundance gives a slightly higher temperature.

The point (3) is understood that increasing the surface gravity increases the atmospheric density, and the higher electron density suppresses ionization (Saha relation; see Figure 1). Consequently, higher temperature is required to achieve the observed ionization state. This relation may be written approximately as $kT_{eff} \propto \log g$.

Effect of the abundance change (point (4) above) may be understood as follows: Abundance variation affects depth of the atmosphere where optical depth reaches unity, such that increasing metal abundances causes the absorption edges to be optically thick at closer to the surface where temperature is lower. Hence the number of high energy photons above the edges decreases. This effect is more significant in the NLTE model, since increasing the abundance makes the atmosphere more opaque due to increase of the mass absorption coefficient (Hartmann and Heise 1997). Therefore, increasing the metal abundance requires a higher effective temperature to account for the observed high energy photons.

3.2. RXJ0925.7–4758

3.2.1. Spectral Analysis with Simple Models

First, we show the result of a blackbody plus interstellar absorption model fit (first column in Table 5 and Figure 6). Although this model does not fit the data at all (reduced χ^2=8), the following spectral characteristics are clearly recognized: (1) The spectrum is heavily absorbed ($N_H \gtrsim 10^{22}$ cm^{-2}); (2) A deep edge feature such as the O VIII edge in CAL87 is *not* observed. (3) The energy spectrum is much harder than that of CAL87 and extends to $\sim$ 1.5 keV. A thin thermal plasma model (Raymond and Smith 1977) gives T= 50 eV, $N_H = 1.98 \times 10^{22}$ cm^{-2}, and a reduced χ^2 of 16. The high absorption and the significant excess above $\sim$ 1.5 keV are model independent. A power-law plus absorption model does not give a meaningful result, ending up with a photon index higher than 10.

We next try a blackbody model with absorption edges. We find that three absorption edges are needed to fit the energy spectrum (Table 5, second column). In addition, if we allow oxygen abundance in the interstellar medium to be free, the fit significantly improves as $\Delta\chi^2 = 53.6$ (Table 5, third column). Figure 7 shows the satisfactory fit by the blackbody plus three edge model with

a reduced oxygen abundance. The first edge at $0.90\pm^{0.02}_{0.03}$ keV may be identified as O VIII or Ne I K-edges at 0.87 keV. Instead of putting a 0.90 keV edge, the spectrum can be fitted equally well by increasing the neon abundance in the interstellar absorption (Table 5, fourth column). The highest edge at $1.36\pm^{0.07}_{0.05}$ keV could be identified with the Ne X edge at 1.36 keV. The 1.02 ± 0.02 keV edge, whose origin is unclear, is close to the energies of the Fe VII L_I-edge (1.03 keV) or Ne VI K-edge (1.04 keV).

The hydrogen column densities ($\sim 1-2\times10^{22}$ cm^{-2}) are consistent with those estimated from optical/IR and ROSAT observations (Motch, Hasinger and Pietsch 1994). The large column density suggests the source is beyond the Vela Sheet molecular cloud at 425 pc (Motch, Hasinger and Pietsch 1994).

3.2.2. Theoretical White-dwarf Models

Next, we try LTE and NLTE white dwarf spectral models (cosmic abundance of the white dwarf atmosphere is assumed). The oxygen and neon abundances in the interstellar absorption are allowed to be free, which will be reasonable from the consideration in the previous section. Results are shown in Table 6 and Figures 8 to 11.

Figures 8 and 9 respectively show examples of the fits with the LTE and NLTE model with a surface gravity of 10^9 cm s^{-2}. These model spectra have very strong O VIII edge at 0.89 keV (LTE model) or Ne IX edge at 1.20 keV (NLTE model), but neither of them is actually observed. In fact, there are significant amounts of hard photons above these edge energies, and the observed spectrum indicates the Ne X edge at 1.36 keV, instead of the Ne IX edge in the NLTE model. A more sophisticated NLTE model including metal line opacities shows weaker Ne IX edge but more conspicuous O VIII edge (Hartmann et al. 1999), rather being similar to the LTE model. Hence, the problem that there are much more high energy photons than predicted by our LTE or NLTE model is unlikely to be solved by further minor improvement of the models.

At the surface gravity 10^9 cm s^{-2}, the maximum effective temperature will be ~ 90 eV (section 3.1.3). On the other hand, the effective temperature has to be as high as ~ 100 eV so that Ne X becomes more dominant than Ne IX (Figure 1). Therefore, expecting a higher temperature and ionization state, we next try models with the surface gravity 10^{10} cm s^{-2}, which would be considered the upper-limit for white dwarfs (Figure 13). The temperature grids are every 10^5 K from 8×10^5 K to 1.9×10^6 K for the LTE model and every 10^4 K from 8×10^5 K to 1.2×10^6 K for the NLTE model. Although models do exhibit Ne X edge, the fit does not improve significantly (Table 6) unless putting an additional edge at ~ 1.02 keV. In Figure 10, 11 and Table 6, we show results of the successful LTE and NLTE model fits with the surface gravity 10^{10} cm s^{-2} and an absorption edge at ~ 1.02 keV.

If the CNO cycle is dominant on the white dwarf surface, it will change the relative abundances of these elements, such that C and O abundances are suppressed relative to that of N. Having this

in mind, we have calculated several LTE and NLTE models with non-standard element abundances. However, we could not fit the RXJ0925.7–4758 spectrum successfully, unless putting the $\sim$ 1.02 keV edge. For example, we have tried a LTE model with [N/C]=200 and [N/O] = 50. The O VII and O VIII edges become weak, which is in the sense to fit the data, but the N VI (0.55 keV) or N VII (0.67 keV) edges are very conspicuous in the model, which are not observed. We have also tried models in which all the heavy element abundances are lowered by an order of magnitude. We have found that reducing the abundance helps to account for the hard-tail above the Ne IX edge, which is in agreement with Shimura (2000). However, the 1.02 keV edge feature still remains in the residual.

We have also tried a two component model, expecting that the hard photons above O VIII and Ne IX edges might be explained by an additional hard component. Hartmann et al. (1999) fitted the RXJ0925.7–4758 spectrum observed with LECS on-board SAX with a NLTE model for the soft component and a thin thermal model for the hard component. We have tried LTE model with $g = 10^{10}$ cm s^{-2} with an additional thin thermal plasma model (Raymond and Smith 1977) for the hard component, according to Hartmann et al. (1999). The results are shown in Table 7 and Figure 12. Although the high energy photons are explained by the hard component as expected, the fit is not as good as the previous ones including the $\sim$ 1.02 keV edge. In fact, we still see the $\sim$ 1.02 keV edge feature clearly in the residual of the fit (Figure 12). Note that ASCA SIS has about twice better spectral resolution than SAX LECS at 1 keV, and residual of the SAX two component fit (Figure 7 in Hartmann et al. 1999) also indicates an edge-like feature at $\sim$ 1 keV. Therefore, we conclude that the $\sim$ 1.02 keV edge is a local feature, and cannot be explained by introducing additional emission component.

4. Discussion

4.1. CAL87

4.1.1. White dwarf parameters

We have applied theoretical LTE and NLTE models to the CAL87 energy spectra observed with ASCA, and obtained effective temperature and emission area. Based on the spectral fitting results, we can constrain white dwarf parameters in CAL87.

Mass and radius of white dwarfs are related by the theoretical white-dwarf mass-radius relation, thus radius and surface gravity are almost uniquely determined as a function of mass. In the bottom panel of Figure 13, we show white dwarf radius and surface gravity as a function of mass, in which we used an approximated formula of the mass-radius relation by Pringle and Webbink (1975). Although the mass-radius relationship is known to be dependent on internal atomic compositions (e.g., Panei, Althaus and Benvenuto 2000), this uncertainty hardly affects our results, since most uncertainties in our discussion originate in the systematic difference of the LTE and NLTE models

and statistical errors from the spectral fitting.

The Eddington luminosity is a function of mass, hence the corresponding maximum effective temperature on the white dwarf surface is also determined solely by mass (section 3.1.3); these are shown in the top and middle panel of Figure 13 respectively.

From model fitting assuming the surface gravity $g = 10^9$ cm s^{-2}, we have obtained effective temperatures. The model spectral shape is hardly dependent on the surface gravity, and best-fit effective temperature varies with the gravity as $kT_{eff} \propto \log g$ (section 3.1.3). This relation is shown for the LTE and NLTE fitting results respectively in the middle panel of Figure 13 by two solid lines. The total bolometric luminosity is calculated as $4\pi\sigma R^2 T_{eff}^4$, using the observed effective temperature and the white dwarf radius derived from the mass-radius relationship, which is also indicated in the top panel by two solid lines for LTE and NLTE models respectively. Note that the intrinsic luminosities thus calculated are much larger than the apparent observed luminosity derived from the observed flux assuming uniform emission, which suggests most of the emission is blocked (see below).

Steady nuclear burning of the hydrogen accreted onto white dwarfs, to be observed as super-soft X-ray sources, takes place only in a limited range of the mass accretion rate, $(1 - 5)\times10^{-7} M_\odot \mathrm{yr}^{-1}$ (van den Heuvel et al. 1992). The allowable luminosity range with the steady nuclear burning calculated by van den Heuvel et al. (1992) is shown as shaded area in the top panel of Figure 13. In this panel, portion of the two lines marked LTE and NLTE lying on the allowable theoretical luminosity range should give the realistic luminosity and mass ranges. They are, $1.0 - 1.2 M_\odot$ and $6 \times 10^{37} - 1.2 \times 10^{38}$ ergs s^{-1} for the LTE model, and $0.8 - 1.0 M_\odot$ and $(4 - 7) \times 10^{37}$ ergs s^{-1} for the NLTE model, respectively. Considering current uncertainties of theoretical spectral models, we conclude the total bolometric luminosity and mass of CAL87 are in the range of $4 \times 10^{37} - 1.2 \times 10^{38}$ ergs s^{-1} and $0.8 - 1.2 M_\odot$, respectively.

In the top panel of Figure 13, we also show the range of the bolometric luminosity calculated from the observed flux assuming uniform emission. We can see that the observed luminosity, 4×10^{36} to 10^{37} erg s^{-1}, is about an order of magnitude smaller than the expected luminosity, indicating that only ~ 10 % of the total emitted X-rays reaches us. This is consistent with, and strengthens the idea by Schmidtke et al. (1993) and Schandl, Meyer-Hofmeister and Meyer (1997) that the white dwarf in CAL87 is permanently blocked from line-of-sight by an outer part of the accretion disk, and we are observing scattering emission by the Accretion Disk Corona (ADC). The scattering optical depth of the corona is estimated as ~ 0.1, which is small enough not to smear the observed deep edge feature (section 3.1.1).

Hydrogen column density of the ADC will be $\sim 1.5 \times 10^{23}$ cm^{-2}, and its size is estimated as $\sim 5 \times 10^{10}$cm (see next section). Correspondingly, the ionization parameter, $\xi = L/(nr^2) \approx L/(N_H r)$ will be 5000 – 16000. This will be large enough to completely photoionize heavy elements besides iron, so that absorption edges are fully eliminated below $\sim$ 8keV (e.g., Kallman and McCray 1982). Hence, the ADC should be observed only as a scatterer, not an absorber, which is consistent with

the present observation (see also discussion in Asai et al. 1998).

4.1.2. Orbital Eclipses

Based on the white dwarf parameters obtained in the previous section, we will try to explain the orbital eclipse in the framework of the ADC model. Namely, a part of the extended emission from ADC is blocked by the companion star, resulting a shallow and extended X-ray eclipse as observed (Schmidtke et al. 1993; Schandl, Meyer-Hofmeister and Meyer 1997). We will carry out Monte Carlo simulation searching for the orbital parameters and ADC configuration to reproduce the observed X-ray orbital light curve.

In our model, parameters which affects the orbital light curve are the following: the white dwarf mass (M_{WD}), companion mass (M_C), size of the ADC, and the orbital inclination angle (i). In the previous section we estimated M_{WD} as 0.8–1.2 $M_\odot$. In the simulation, we assume $M_{WD} = 1M_\odot$. M_C is expected to be in the range of 1.4 $M_\odot$ to 2.2 $M_\odot$ from the binary evolution requirements (van den Heuvel et al. 1992); we assume $M_C = 1.5M_\odot$. The orbital period is 10.6 hr (Alcock et al. 1997 and references therein), and the binary separation is determined from the Kepler's law as $a = 2.3 \times 10^{11}$ cm. The Roche lobe radius is calculated using the formula by Pringle (1985), and we consider that the companion is filling its Roche lobe. Roche radius for the companion and white dwarf will be 0.41 times and 0.34 times the binary separation, respectively. Accretion disk radius is assumed to be 0.8 times the white dwarf Roche lobe radius, following Schandl, Meyer-Hofmeister and Meyer (1997). The ADC is assumed to be a sphere whose radius is smaller than the accretion disk radius. The white dwarf is permanently blocked from the line-of-sight by the outer flared parts of the disk or the "spray" region (Schandl, Meyer-Hofmeister and Meyer 1997). This is approximated by that the disk is a slab having a constant thickness 0.2 times the disk radius. Also disk is assumed not to be tilted from the orbital plane.

We have carried out Monte Carlo simulations for many different combinations of these parameter values, and found that the orbital light curve is most strongly dependent on the orbital inclination, and secondly on the ADC size. In particular, we have found that depth of the eclipse is very sensitive to the inclination, since in our model a tiny portion of the ADC has to be seen just behind the companion (see the diagram at $\phi = 1$ in Figure 14). Dependence on other parameters is relatively minor. In any case, it is impossible to constrain orbital parameters from our simulation, since there are too many combinations which can reproduce the observed X-ray light curve, which is rather noisy.

As a typical example of successful orbital simulation, we show the result with the ADC size 4.8×10^{10} cm (= 0.75 times the accretion disk radius), and $i = 73°$ (Figure 14). Schandl, Meyer-Hofmeister and Meyer (1997) carried out orbital simulation, and successfully explained the observed optical light curve with $i = 77°$. We have reached $i = 73°$, having searched for the best inclination angle around $i = 77°$ to fit the observed X-ray light curve.

Several remarks should be made here on our simulation: If we compare closely, the observed eclipse is slightly wider than the simulation (Figure 14). We assumed that the ADC has constant emissivity and did not take into account the rim darkening, inclusion of which should further narrow the simulated eclipse. Our choice of the ADC size (0.75 times the disk radius) is rather arbitrary, but if the ADC size becomes smaller than half the disk radius, the eclipse will be still narrower and very fine tuning of the inclination will be required so that the eclipse takes place. Hence, our model favors a large ADC size. Also there expects to be additional mechanisms to widen the eclipse which we have not taken into account. For example, we assumed that the companion is a perfect sphere with definite boundaries, but in reality the companion filling the Roche lobe should be elongated toward the white dwarf, which can block the ADC more effectively and make the eclipse wider. In addition, the companion may have an extended atmosphere and/or winds to attenuate X-rays by scattering, which also will work to widen the eclipse (Asai et al. 1998). Future high throughput observations will allow more precise X-ray eclipse analysis to constrain the binary parameters tightly.

4.2. RXJ0925.7–4758

We have found that the RXJ0925.7–4758 spectrum has high energy photons above O VIII or Ne IX edge energies and exhibits the Ne X edge at 1.36 keV. Such a hot atmosphere, as high as $T_{eff} \sim 100$ eV (Tables 6), requires an extremely high surface gravity, $g \approx 10^{10}$ cm s^{-2}, which may be achieved only at close to the Chandrasekhar limit, $\sim 1.4 M_{\odot}$ (Figure 13; see also Hoshi 1998; Shimura 2000). Presence of such an extremely massive white dwarf is also consistent with optical observations of the binary motion. (Schmidtke et al. 2000).

We have found that the model fits always require an additional absorption edge at ~ 1.02 keV. This edge feature does not disappear by introducing second high energy spectral component (Figure 12), which was proposed by Hartmann et al. (1999) to explain the SAX RXJ0925.7–4758 spectrum.

Near the Chandrasekhar limit, the X-ray luminosity expected from the steady nuclear burning will be as high as (1–2)$\times 10^{38}$erg s^{-1} (Figure 13). On the other hand, the luminosity we obtained from the LTE or NLTE model fitting ($g \approx 10^{10}$ cm s^{-2}, including the 1.02 keV edge) is (3–4)$\times 10^{34}$erg s^{-1} at 1 kpc. Even if we put the source at ~ 10 kpc, discrepancy between the expected and observed luminosities is still almost two orders or magnitude. We have found that the observed luminosity of CAL87 is just 10 % of the expected total luminosity (section 4.1.1), which we consider because the white dwarf is always hidden by the accretion disk. Blocking by the accretion disk will be unlikely for RXJ0925.7–4758 though, since neither X-ray or optical eclipses has been detected, and the orbital inclination is considered to be much smaller (Motch 1998; Schmidtke 2000).

To solve the luminosity discrepancy, we propose a model that the white dwarf in RXJ0925.7–4758 is behind a non-uniform, almost fully ionized Thomson thick cloud, so that heavy electron

scattering causes the significant luminosity reduction. Since the cloud is not spherical, photons scattered out of the line of sight will never be observed again. The 1.02 keV absorption edge and the strong low energy absorption may be explained simultaneously, if ionization state of the cloud in the line of sight is not uniform, so that less ionized part of the cloud is responsible for these absorptions. A transient optical jet has been observed from RXJ0925.7–4758 (Motch 1998). Therefore, we consider it likely that matter previously emitted as the jet from the binary system lies in the line of sight to scatter the X-rays from the white dwarf.

We consider the observed luminosity, $\sim 3\times10^{34}(d/1\ \mathrm{kpc})^2$, is $e^{-\tau_{sct}}$ times the actual luminosity, $\sim 10^{38}$ erg s^{-1}, where τ_{sct} is the scattering optical depth of the intervening matter. Hence, column density of the intervening matter may be written as,

$$N_H \sim \{12 - 7\log(d/1\ \mathrm{kpc})\} \times 10^{24}\mathrm{cm}^{-2}. \tag{1}$$

On the other hand, time average of the mass ejection rate due to the jet is,

$$< dM/dt >= 4\pi r^2 vn(\delta/4\pi)wm_H, \tag{2}$$

where v is the jet velocity, n the number density, w the time fraction when the jet takes place, δ solid angle, and m_H is the mass per hydrogen atom. The column density can be also written as,

$$N_H = \int_R^\infty nwdr = \frac{< dM/dt >}{Rv\delta m_H}, \tag{3}$$

where R is the white dwarf radius. From these relationships, we get,

$$< dM/dt > \sim 3 \times 10^{17} \left(\frac{R}{3000\ \mathrm{km}}\right) \left(\frac{v}{5000\ \mathrm{km/s}}\right) \left(\frac{\delta}{1}\right) \{12 - 7\log\,(d/1\ \mathrm{kpc})\}\ \mathrm{g\,s^{-1}}, \tag{4}$$

where plausible values of v and δ are taken from Motch (1998).

Only constraint we may impose is that the mass ejection rate does not exceed the plausible mass accretion rates for the super-soft sources, $\sim 10^{19}$ g s^{-1} (e.g., van den Heuvel et al. 1992). From equation 4, we see that this condition is satisfied as long as $d \gtrsim 1$ pc; hence we may not constrain the distance to the source. For an assumed distance of 1 kpc, 3 kpc and 10 kpc, the column density of the intervening matter necessary to reduce the luminosity will be $\sim 1 \times 10^{25}$, $\sim 9 \times 10^{24}$, $\sim 5 \times 10^{24}$ cm^{-2} respectively, and the mass ejection rate is $\sim 4 \times 10^{18}$, $\sim 3 \times 10^{18}$ and $\sim 2 \times 10^{18}$ g s^{-1}.

Ionization parameter of the matter may be written as,

$$\xi = \frac{L}{nr^2} = \frac{Lw}{N_H R}$$

$$\sim 1200 \frac{(L/10^{38}\ \mathrm{erg\ s^{-1}})(w/0.04)}{(N_H/10^{25}\ \mathrm{cm^{-2}})(R/3000\ \mathrm{km})}, \tag{5}$$

where we took the jet frequency $w \sim 0.04$, as the jet was observed in one out of 23 nights (Motch 1998). The plasma is almost fully ionized, that it is transparent for low energy absorption, but works just as a scatterer to reduce the observed luminosity. The jet frequency may not be uniform, and there may be a period when w is small and a particularly dense material is ejected. In that case, the radial region corresponding that dense matter will have locally a lower ionization state. The 1.02 keV edge may originate in moderately ionized heavy elements such as Ne or Fe in such a low-ionized region.

5. Conclusion

We have observed the super soft sources CAL87 and RXJ0925.7–4758 with ASCA SIS, and carried out precise spectral analysis. Thanks to the superior energy resolution of SIS ($\Delta E/E \sim 10\%$ at 1 keV) compared to previous instruments, we could study detailed X-ray spectral structure of these sources for the first time. Important results are summarized in the following:

(1) We have applied theoretical spectral models to CAL87, and constrained the white dwarf mass and intrinsic luminosity as $0.8 - 1.2 M_{\odot}$ and 4×10^{37}–1.2×10^{38} erg s^{-1}, respectively. We have found the observed luminosity is an order of magnitude smaller than the intrinsic luminosity, which indicates the white dwarf is permanently blocked by the accretion disk and not directly seen. This strongly suggests that we are observing a scattering emission by a fully ionized accretion disk corona (ADC) whose column density is $\sim 1.5 \times 10^{23}$ cm^{-2}.

(2) Through simulation, we have shown that the orbital eclipse can be explained by the ADC model, such that a part of the extended X-ray emission from the ADC, whose size is expected to be ~ 75 % of the accretion disk radius, is blocked by the companion star filling its Roche lobe. The orbital inclination angle is $\sim 73^{\circ}$ to explain the observed eclipse profile.

(3) In order to explain the RXJ0925.7–4758 spectrum, very high surface gravity and temperature, $\sim 10^{10}$ cm s^{-2} and $\sim$100 eV respectively, are required. These values are only possible for an extremely heavy white dwarf near the Chandrasekhar limit. Therefore, RXJ0925.7–4758 may be an immediate progenitor of Type Ia supernovae, which has been long-sought (e.g., Livio et al. 1996). We have found the energy spectrum has a ~ 1.02 keV edge, which may be a composite of mildly ionized L- or K-edges of heavy elements.

(4) Although super-soft sources should have the luminosity $\sim 10^{38}$ erg s^{-1} at the Chandrasekhar limit, the observed luminosity from RXJ0925.7–4758 is smaller by more than two orders of magnitude. To explain the luminosity discrepancy, we propose a model that very thick matter (as much as $\sim 10^{25}$ cm^{-2}) which was previously ejected from the system as jets intervenes the line of sight, and reduces the luminosity significantly due to Thomson scattering. We have shown that the matter is almost fully ionized that it is transparent for soft X-ray photons. Some radial portion of the ejected matter, where ionization state is locally low and heavy elements are not fully ionized, may be origin of the significant low energy absorption and the ~ 1.02 keV edge.

We wish to thank the anonymous referee for his/her carefully reading the manuscript and useful comments.

REFERENCES

Alcock C. et al. 1997, MNRAS, 287, 699

Anders, E. and Ebihara, M. 1982, Geochimica et Cosmochimica Acta, 46, 2363

Arnaud, K.A., 1996, Astronomical Data Analysis Software and Systems V, eds. Jacoby G. and Barnes J., p17, ASP Conf. Series volume 101.

Asai, K., Dotani, T., Nagase, F., Ebisawa, K., Mukai, K., Smale, A. P. and Kotani, T. 1998, ApJ, 503, L143

Barman, T. S. et al. 2000, ApJ, 537, 946

Cowley, A. P., Schmidtke, P. C., Crampton, D. and Hutchings, J. B. 1990, ApJ, 350, 288

Dennefeld, M., 1989, in "Recent Developments of Magellanic Cloud Research. A European Colloquium", Ed. K.S. de Boer, F. Spite and G. Stasinska, Observatoire de Paris, Section Astrophysique de Meudon, Meudon, France, p. 107

Deutsch, E. W., Margon, B., Wachter, S., Anderson, S. F. 1996, ApJ, 471, 979

Ebisawa K. et al. 1996, in "Supersoft X-ray Sources", ed. J. Greiner, Springer, p.91

Hartmann, H. W. and Heise, J. 1997, A&A, 322, 591

Hartmann, H. W. et al. 1999, A&A, 346, 125

Heise, J., van Teeseling, A. and Kahabka, P. 1994, A&A, 288, L45

Hoshi, R. 1998, PASJ, 50, 501

Long, K. S., Helfand, D. J. and Grabelsky, D. A. 1981, ApJ, 248, 925

Kahabka, P. and van den Heuvel, E. P. J. 1997, ARA&A, 35, 69

Kahabka, P., Pietsch, W. and Hasinger, G. 1994, A&A, 288, 538

Kallman, T. R. and McCray, R. 1982, ApJS, 50, 263

Livio, M. 1996, in "Supersoft X-ray Sources", ed. J. Greiner, Lecture Note in Physics, 472, p. 183, Springer

Motch, C., Hasinger, G. and Pietsch, W. 1994, A&A, 284, 827

Motch, C. 1996, in "Supersoft X-ray Sources", ed. J. Greiner, Lecture Note in Physics, 472, p. 83, Springer

Motch, C. 1998, A&A 338, L13

Panei,J.A. and Althaus, L.G. and Benvenuto, O.G. 2000, A&A, 353, 970

Pringle, J. E. and Webbink, R. F. 1975, MNRAS, 172, 493

Pringle, J. E. 1985 in "Interacting Binary Star", ed. Pringles, J. E. and Wade, R. A., Cambridge University Press, p. 1

Rauch, T. A&A, 320, 237

Raymond, J. C. and Smith, M. W. 1977, ApJS, 35, 419

Schandl, S., Meyer-Hofmeister, E. and Meyer, F. 1997, A&A, 318, 73

Schmidtke, P. C., McGrath, T. K., Cowley, A. P. and Frattare, L. M. 1993, PASP, 105, 863

Schmidtke, P. C. et al. 2000, AJ, 120, 935

Shimura, T. 2000, MNRAS 315, 345

Tanaka, Y., Inoue, H. and Holt, S. S. 1994, PASJ, 46, L37

van den Heuvel, E. P. J., Bhattacharya,. D., Nomoto, K. and Rappaport, S. A. 1992 A&A, 262, 97

van Teeseling, A., Heise, J., Kahabka, P. 1996, in "Compact Stars in Binaries", IAU Symp. 165, Eds, van Paradijs et al. Kluwer Academic Publishers

Vassiliadis, E. and Wood, P. R. 1994, ApJS, 92, 125

Table 1: CAL87 blackbody plus edges model fit for the average spectrum

$N_H[10^{21}\mathrm{cm}^{-2}]$		$7.7\pm^{5.4}_{4.3}$	3.8 ± 0.5
T [eV]		$53\pm^{26}_{14}$	75 (fixed)
Edge1	E_{edge} [keV]	0.739 (fixed)	0.739 (fixed)
	τ	0.49 ± 0.37	0.73 ± 0.30
Edge2	E_{edge} [keV]	0.871 (fixed)	0.871 (fixed)
	τ	10.0 (fixed)	10.0 (fixed)
$(R/10^3 \mathrm{\ km})^{2\dagger}$		3 – 2100000	$9.2\pm^{2.9}_{2.2}$
L_{bol} $[10^{36}$ erg/s$]^\dagger$		15 – 630000	$38\pm^{12}_{10}$
χ^2/dof		21.9 (31)	23.9 (32)

†The distance is assumed to be 55 kpc.

Note. — Absorption edge of the form $\exp(-\tau(E/E_{\rm edge})^{-3})$ (for $E > E_{\rm edge}$) is assumed.

Table 2: CAL87 LTE model fit: log g=9, LMC abundance.

	All	Eclipse		Out of Eclipse	
$N_H[10^{21}\mathrm{cm}^{-2}]$	2.0±0.7	fixed	2.5±0.2	fixed	1.95±0.09
T_{eff} [eV]	75±1	fixed		fixed	
$(R/10^3 \mathrm{\ km})^2$ †	$1.6\pm^{0.9}_{0.6}$	1.34±0.11	fixed	1.67±0.08	fixed
L_{bol} $[10^{36}$ erg/s$]$ †	$6.6\pm^{3.6}_{2.5}$	5.5±0.5	fixed	6.8±0.3	fixed
χ^2/dof	39.0/32	34.7/34	33.3/34	29.4/34	29.0/34

†The distance is assumed to be 55 kpc.

Table 3: CAL87 NLTE model fit: log g=9, LMC abundance.

	All	Eclipse		Out of Eclipse	
$N_H[10^{21}\mathrm{cm}^{-2}]$	2.0±0.6	fixed	$2.4\pm^{0.2}_{0.1}$	fixed	1.95 ± 0.09
T_{eff} [eV]	58±1	fixed		fixed	
$(R/10^3 \mathrm{\ km})^2$ †	$4.5\pm^{2.4}_{2.7}$	3.7±0.3	fixed	4.7±0.2	fixed
L_{bol} $[10^{36}$ erg/s$]$ †	$6.6\pm^{3.4}_{4.0}$	5.4±0.5	fixed	6.9±0.3	fixed
χ^2/dof	23.1/32	34.6/34	33.9/34	14.6/34	14.3/34

†The distance is assumed to be 55 kpc.

Table 4: CAL87 average spectrum model fit with the cosmic abundance and different surface gravities.

	LTE model		NLTE model	
log g (CGS)	9	10	9	10
$N_H[10^{21}\mathrm{cm}^{-2}]$	2.2±0.9	1.8±0.8	2.2±0.7	$1.2\pm^{1.0}_{0.5}$
T_{eff} [eV]	$75\pm^{2}_{1}$	$89\pm^{2}_{1}$	65±1	79±2
$(R/10^3$ km$)^2$ †	2.1±1.2	$0.71\pm^{0.50}_{0.33}$	$3.3\pm^{2.7}_{1.8}$	$0.66\pm^{0.71}_{0.20}$
L_{bol} [10^{36} erg/s] †	8.6 ± 4.4	$5.8\pm^{4.0}_{2.4}$	$7.7\pm^{5.5}_{4.0}$	$3.4\pm^{2.9}_{0.5}$
χ^2/dof	41.4/32	42.8/32	25.2/32	28.7/32

†The distance is assumed to be 55 kpc.

Table 5: RXJ0925.7–4758 blackbody (plus edges) model fit

$N_H[10^{22}\mathrm{cm}^{-2}]$		2.0	1.14	1.06±0.13	1.09 ± 0.11
T [eV]		45	88	$92\pm^{8}_{10}$	$88\pm^{10}_{6}$
Edge1	E_{edge} [keV]	—	0.86	$0.90\pm^{0.02}_{0.03}$	—
	τ		1.17	0.81 ± 0.3	
Edge2	E_{edge} [keV]	—	1.01	1.02 ± 0.02	$1.01\pm^{0.01}_{0.02}$
	τ		2.35	$1.64\pm^{0.3}_{0.4}$	1.74 ± 0.3
Edge3	E_{edge} [keV]	—	1.31	$1.36\pm^{0.07}_{0.05}$	$1.36\pm^{0.09}_{0.07}$
	τ		1.18	$0.83\pm^{0.7}_{0.6}$	0.68 ± 0.6
Oxygen abundance[a]		1 (fixed)	1(fixed)	0.61±0.1	0.65±0.1
Neon abundance[a]		1 (fixed)	1(fixed)	1 (fixed)	2.3 ± 0.5
R^2 [km^2] †		3.34×10^{10}	22.9×10^4	$5.2\pm^{19}_{4} \times 10^4$	$9.60 \pm^{26}_{7} \times 10^4$
L_{bol} [erg/s] †		1.8×10^{40}	1.8×10^{36}	$4.8\pm^{9}_{3} \times 10^{35}$	$7.5 \pm^{13}_{4} \times 10^{35}$
χ^2/dof		605 (75)	102.8 (69)	49.2 (68)	50.8 (69)

†The distance is assumed to be 1 kpc.

[a]Abundances for the interstellar absorption, relative to the cosmic abundances [O]/[H]=7.39×10^{-4} and [Ne]/[H]=1.38×10^{-4} by Anders and Ebihara (1982). The same definition for the following Tables.

Note. — Absorption edge of the form $\exp(-\tau(E/E_{\rm edge})^{-3})$ (for $E > E_{\rm edge}$) is assumed.

Table 6: RXJ0925.7–4758 LTE and NLTE model fit results.

	LTE			NLTE		
log g (CGS)	9	10	10	9	10	10
N_H [10^{21} cm^{-2}]	21.1	16.5	7.1±0.6	8.7	8.5	$6.9\pm^{0.6}_{0.2}$
Oxygen abundance	0.92	0.90	0.56±0.14	0.65	0.62	0.61±0.15
Neon abundance	0.33	0	$0.56\pm^{0.9}_{0.56}$	2.2	0.26	$4.0\pm^{0.3}_{0.5}$
Edge E_{edge} [keV]	—	—	1.02 ± 0.01	—	—	1.01 ± 0.01
Edge τ			2.1 ± 0.3			$1.72\pm^{0.10}_{0.16}$
T_{eff} [eV]	70	86	$117\pm^{4}_{2}$	74	92	103[a]
R^2 [km^2] †	2.6×10^8	3.3×10^6	$1.26 \pm^{0.28}_{0.35} \times 10^3$	2.7×10^4	7.7×10^3	2.6×10^3
L_{bol} [ergs s^{-1}] †	8×10^{38}	2.3×10^{37}	3.1×10^{34}	1×10^{35}	7×10^{34}	3.8×10^{34}
χ^2 (dof)	288 (73)	288 (73)	79.2 (71)	393 (73)	343 (73)	51.7 (73)

†The distance is assumed to be 1 kpc.

[a]103 eV (= 1.2×10^6 K) is the highest available temperature in the model.

Table 7: RXJ0925.7–4758 LTE plus Raymond and Smith (1977) plasma model fit result

log g (CGS)	10
N_H [10^{21} cm^{-2}]	12.7
Oxygen abundance	0.67
Neon abundance	0.68
T_{eff} [eV]	94
R^2 [km^2] †	7×10^4
T [eV][a]	103
N[b]	1.5×10^{53}
χ^2 (dof)	144 (71)

†The distance is assumed to be 1 kpc.

[a]Plasma temperature.

[b]The plasma emission measure $n_e n_H V$ [cm^{-3}] at 1 kpc, where n_e, n_H and V are electron density, hydrogen density and volume, respectively.

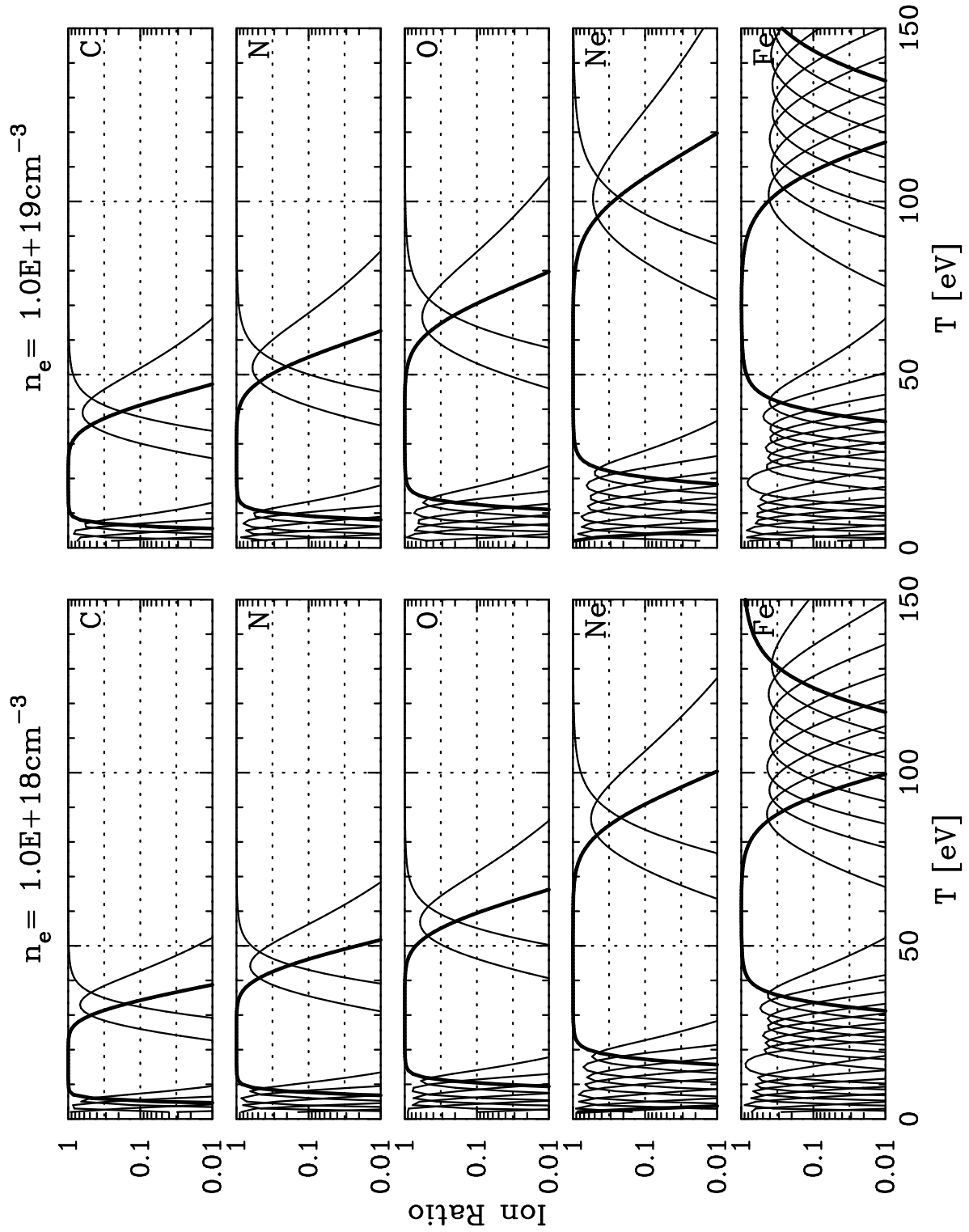

Fig. 1.— Ion Fractions of the major heavy elements as a function of the temperature for the two electron densities 10^{18} and 10^{19} cm^{-3}. LTE condition is assumed. Fractions of the helium-like ions and neon-like ion (for iron) are indicated with the thick lines.

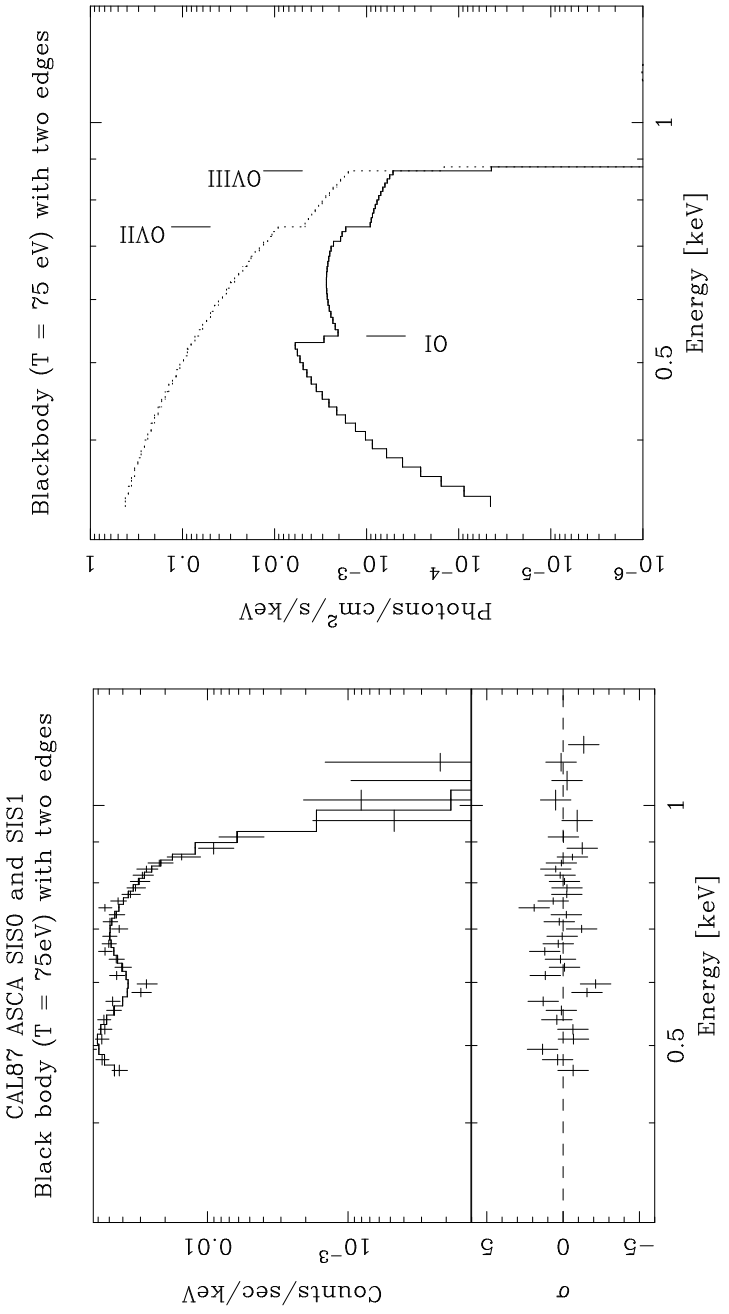

Fig. 2.— Blackbody (T=75 eV) plus two edge model fit for CAL87. Left: Observed spectrum and best-fit model convolved with the detector response. Residuals from the best-fit model are shown in the lower panel. Right: The unfolded best-fit model spectra are shown with (solid line) and without (dashed line) taking into account the interstellar absorption.

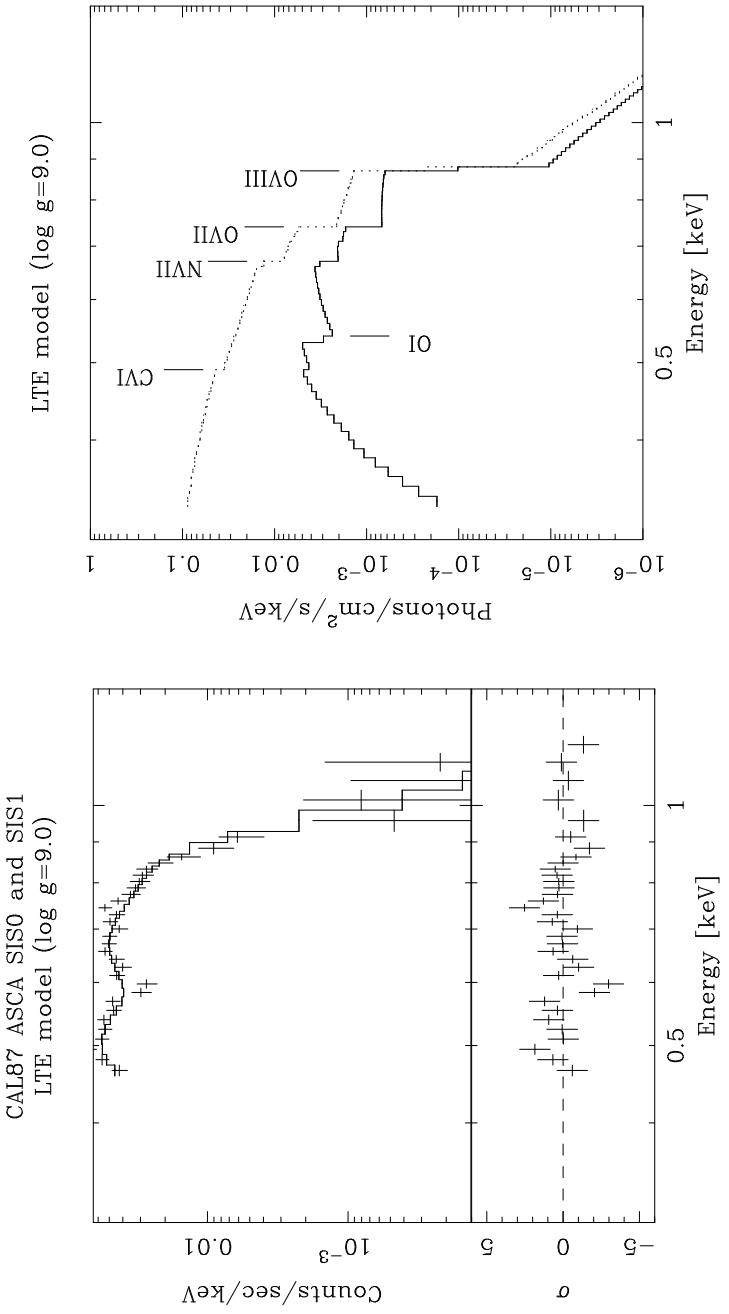

Fig. 3.— LTE model fit for CAL87. Left: Observed spectrum and the best-fit model convolved with the detector response. Right: The best-fit model before and after the interstellar absorption. Absorption edges in the model and those due to the interstellar absorption are indicated. Note that energies of the O VIII and Ne I edges coincide (0.87 keV).

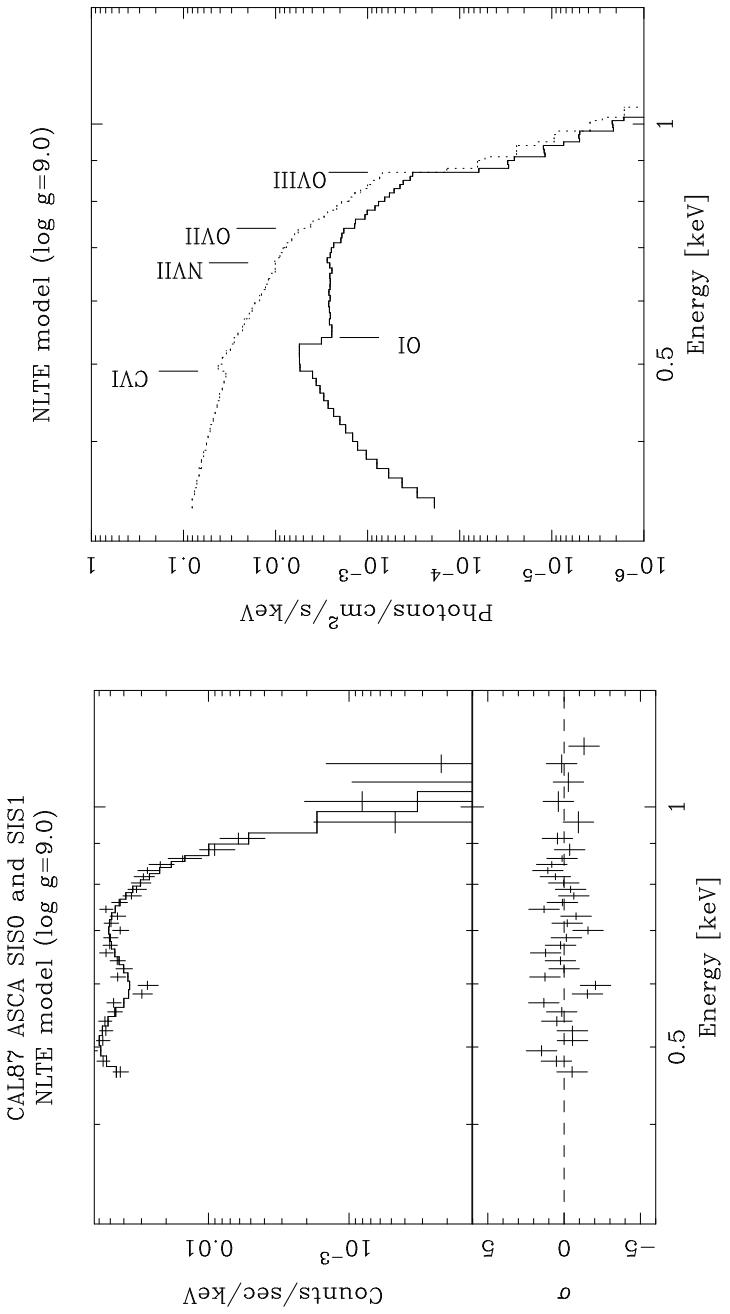

Fig. 4.— NLTE model fit for CAL87. Left: Observed spectrum and the best-fit model convolved with the detector response. Right: The best-fit model before and after the interstellar absorption. Absorption edges in the model and those due to the interstellar absorption are indicated.

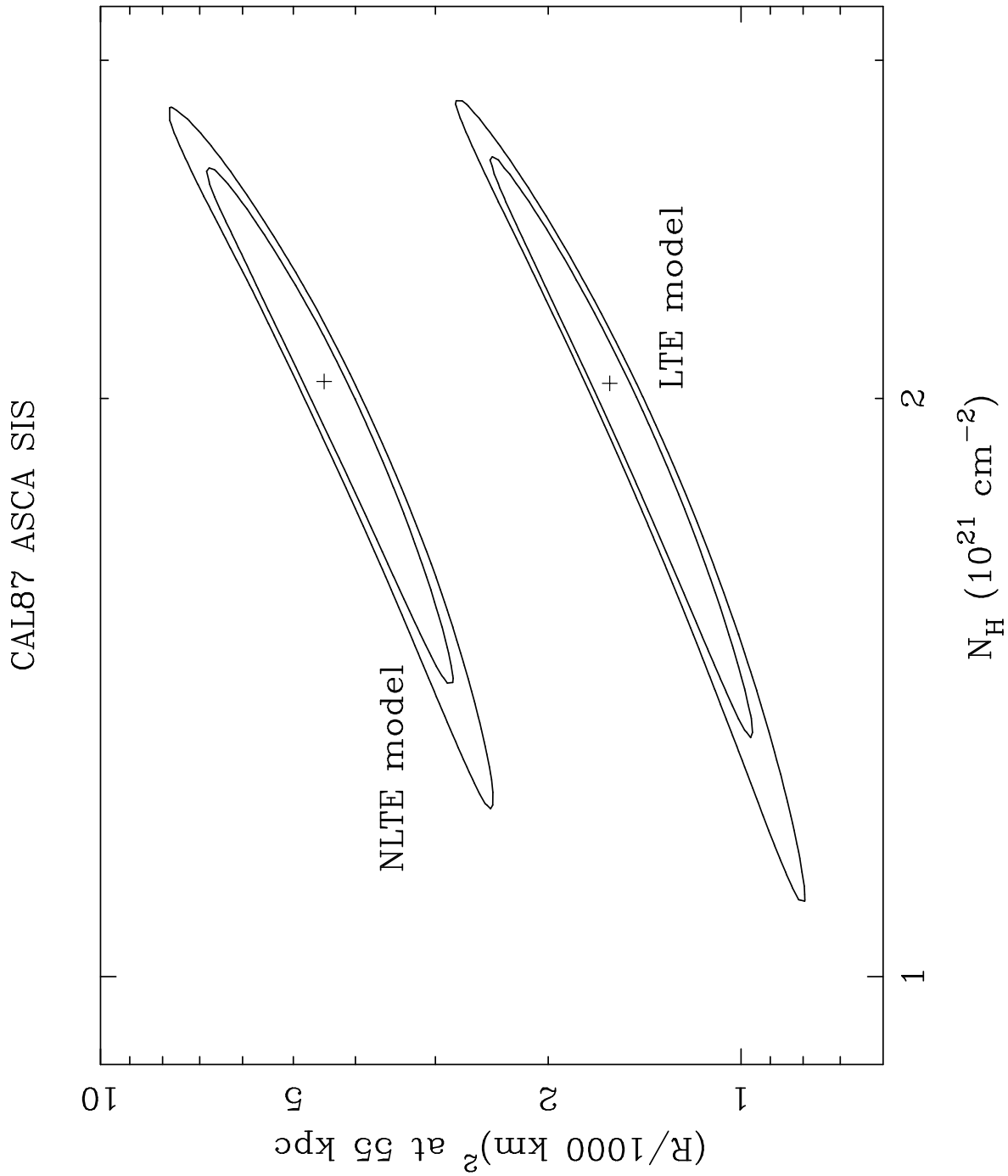

Fig. 5.— Confidence limits of the hydrogen column density and the normalization (converted to the effective emission area at 55 kpc assuming the isotropic emission) for the CAL87 LTE and NLTE model fits. The two contours levels indicate the single parameter 90 % confidence limit ($\chi^2_{min}+2.7$) and the two parameter 90 % confidence limit ($\chi^2_{min}+4.6$).

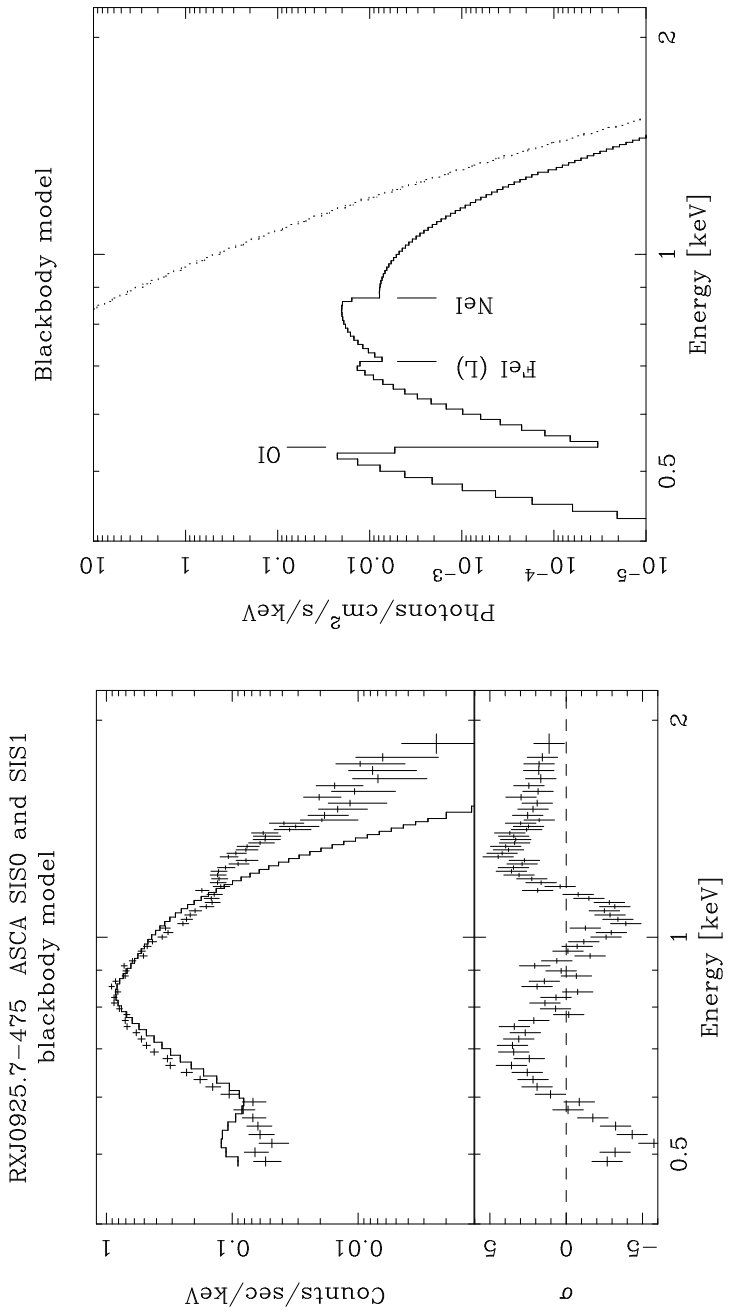

Fig. 6.— Blackbody model fit for RXJ0925.7–4758. Left: Observed spectrum and best-fit model convolved with the detector response. The fitting residual is also shown. Right: The best-fit model before and after the interstellar absorption.

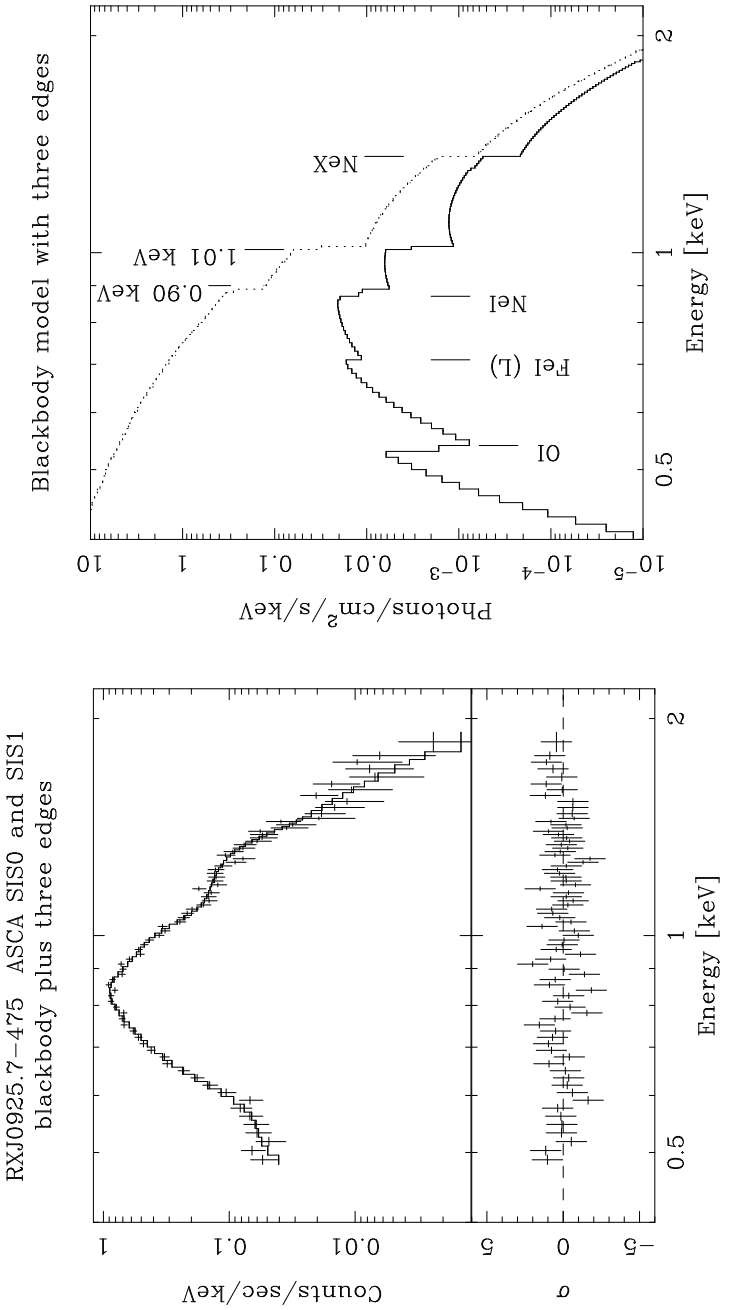

Fig. 7.— Blackbody plus edge model fit for RXJ0925.7–4758. Three edges are included at 0.89 keV, 1.01 keV and 1.36 keV. The oxygen abundance in the interstellar absorption is reduced than the cosmic abundance (see the text). Left: Observed spectrum and best-fit model convolved with the detector response. The fitting residual is also shown. Right: The best-fit model before and after the interstellar absorption.

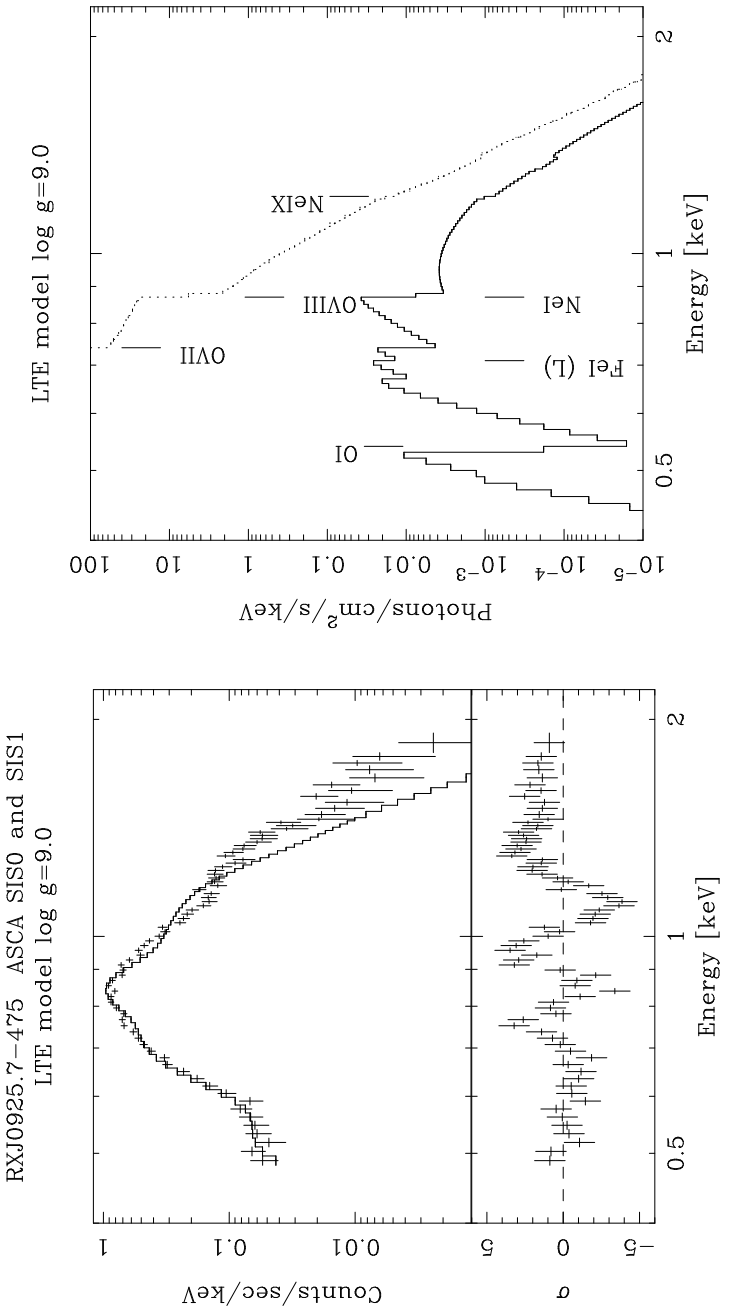

Fig. 8.— LTE model fit for RXJ0925.7–4758 with the surface gravity 10^9 cm s^{-2}. The oxygen and neon abundances in the interstellar absorption are made free parameters (see the text). Left: Observed spectrum and best-fit model convolved with the detector response. The fitting residual is also shown. Right: The best-fit model before and after the interstellar absorption.

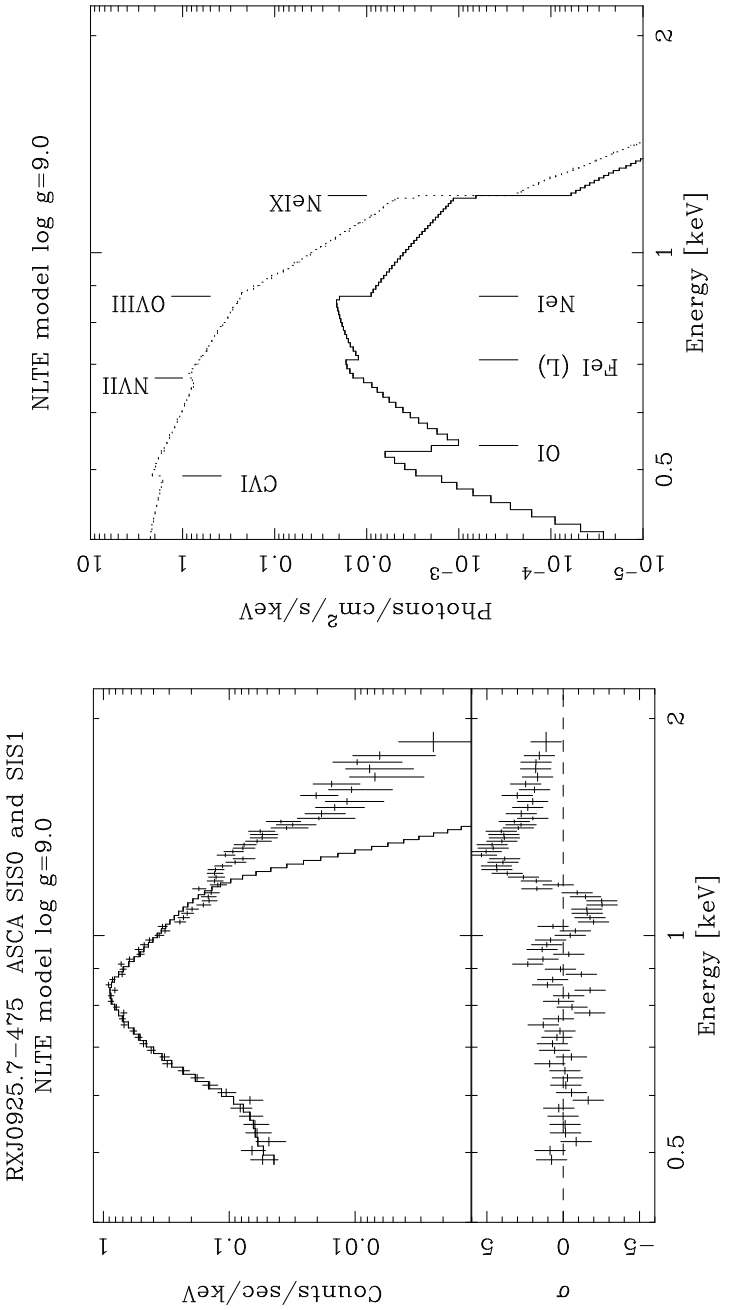

Fig. 9.— NLTE model fit for RXJ0925.7–4758 with the surface gravity 10^9 cm s^{-2} and the cosmic abundance. The oxygen and neon abundances in the interstellar absorption are made free parameters (see the text). Left: Observed spectrum and best-fit model convolved with the detector response. The fitting residual is also shown. Right: The best-fit model before and after the interstellar absorption.

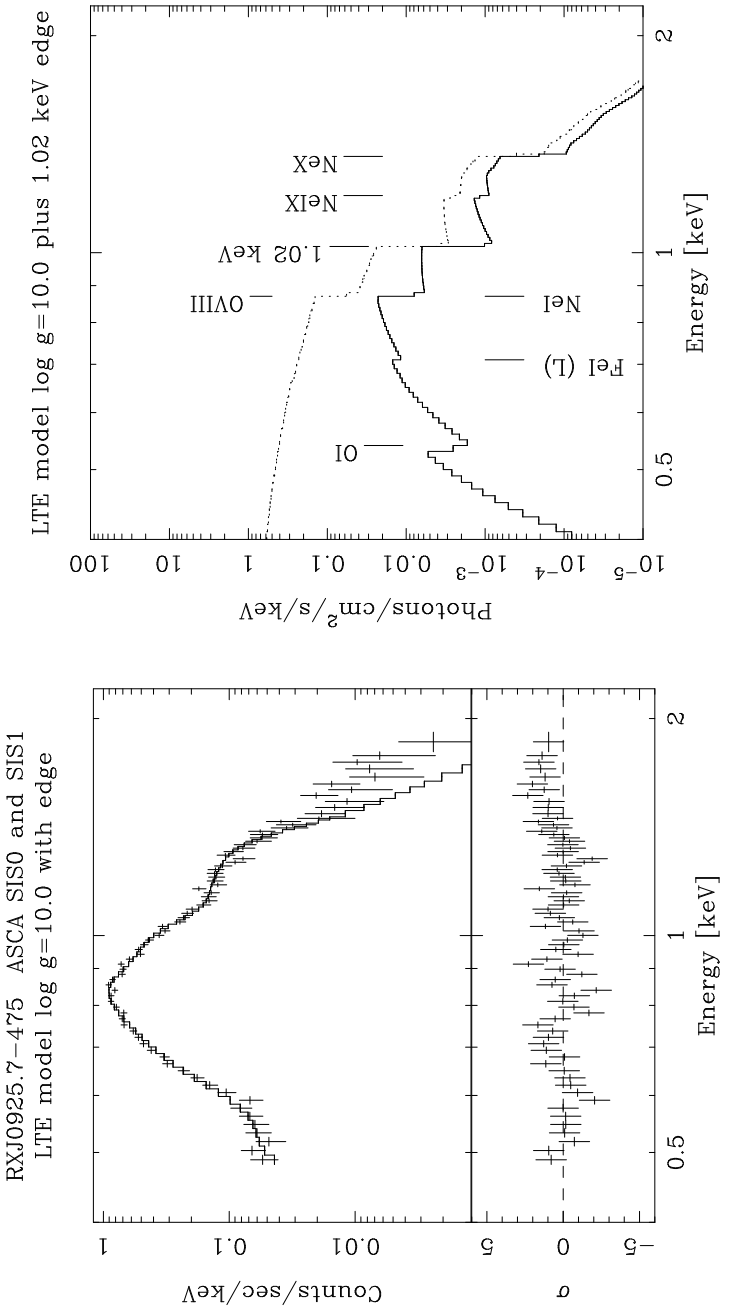

Fig. 10.— LTE model fit for RXJ0925.7–4758 with the surface gravity 10^{10} cm s^{-2} and an absorption edge at 1.02 keV. The oxygen and neon abundances in the interstellar absorption are made free parameters (see the text). Left: Observed spectrum and best-fit model convolved with the detector response. The fitting residual is also shown. Right: The best-fit model before and after the interstellar absorption.

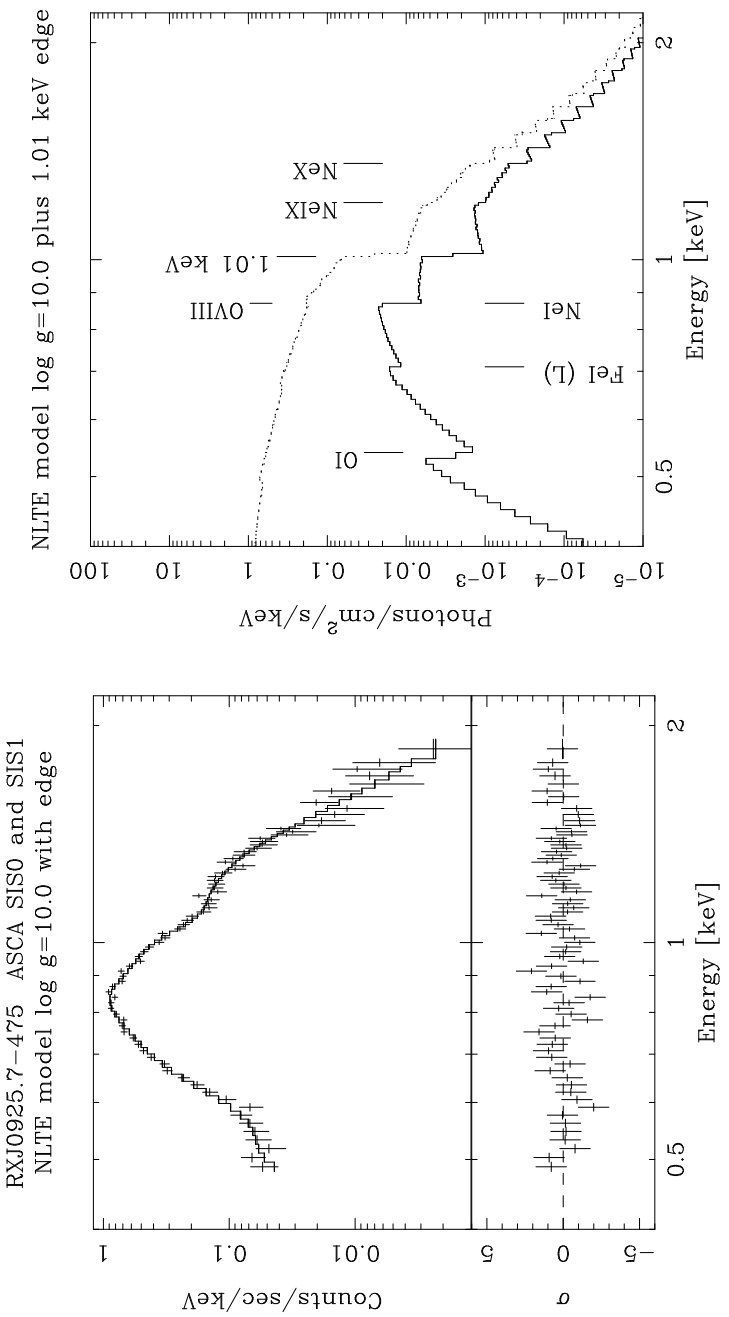

Fig. 11.— NLTE model fit for RXJ0925.7–4758 with the surface gravity 10^{10} cm s^{-2} with an absorption edge at 1.01 keV. The oxygen and neon abundances in the interstellar absorption are made free parameters (see the text). Left: Observed spectrum and best-fit model convolved with the detector response. The fitting residual is also shown. Right: The best-fit model before and after the interstellar absorption.

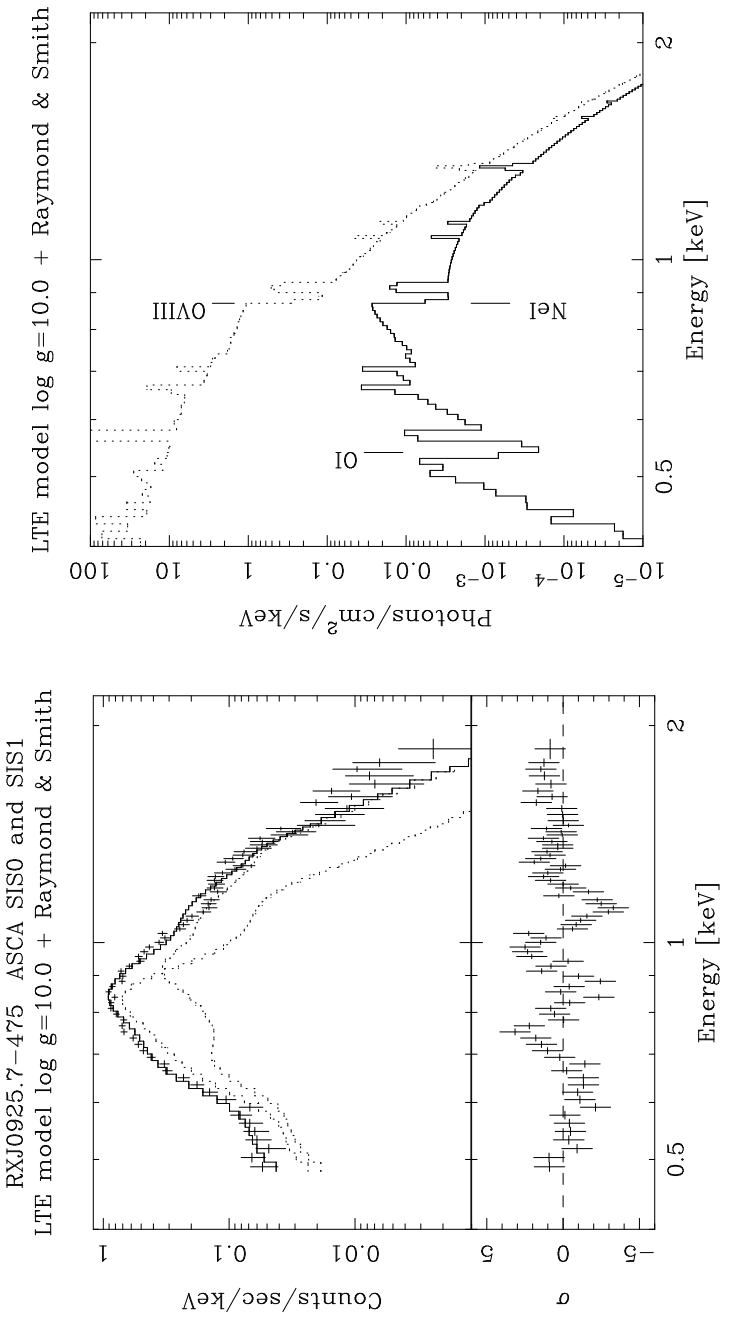

Fig. 12.— LTE model (surface gravity 10^{10} cm s^{-2}) plus Raymond & Smith plasma model fit for RXJ0925.7–4758. The oxygen and neon abundances in the interstellar absorption are made free parameters (see the text). Left: Observed spectrum and best-fit model convolved with the detector response. The fitting residual is also shown. Right: The best-fit model before and after the interstellar absorption.

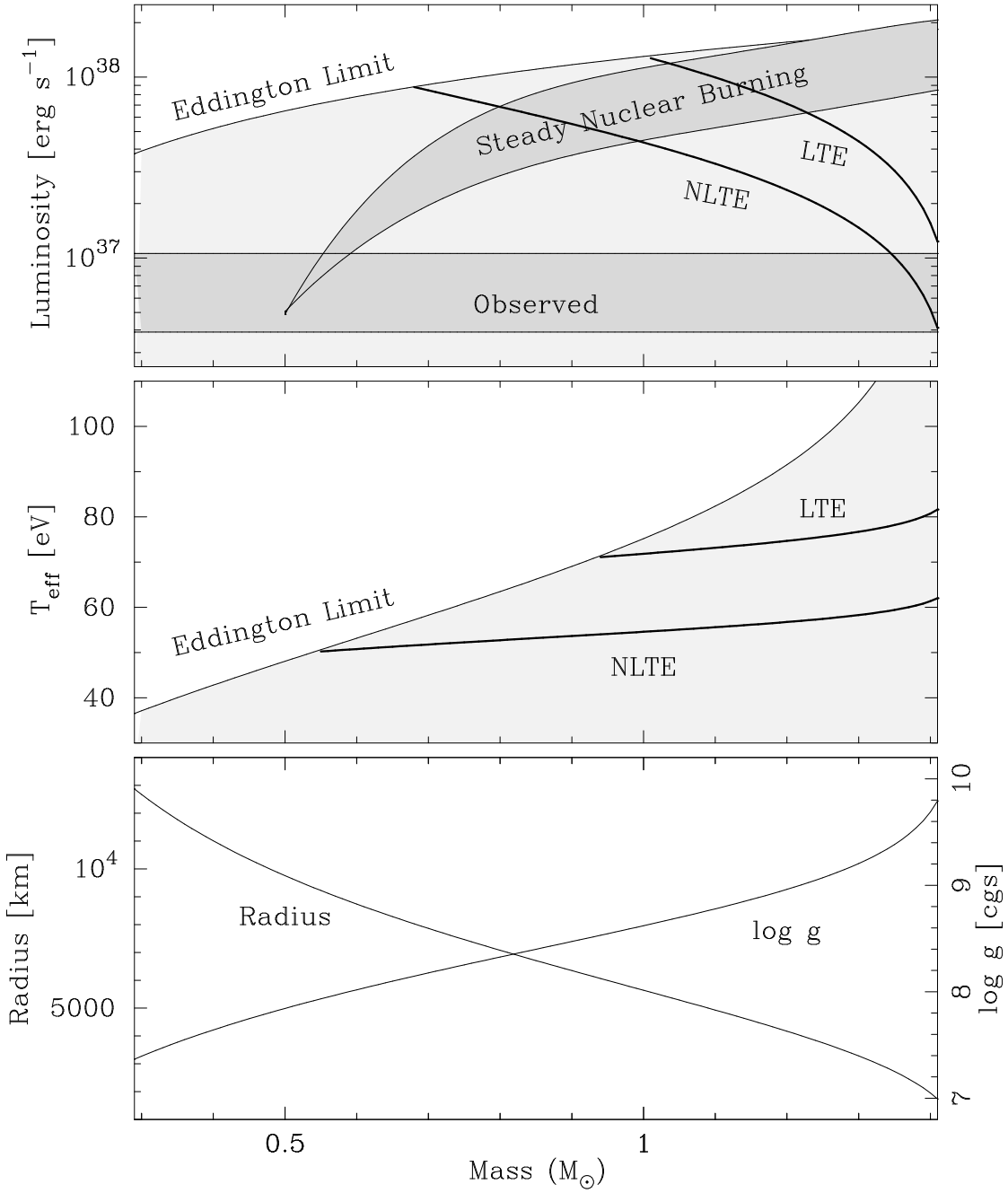

Fig. 13.— Radius, surface gravity and the maximum effective temperatures at the Eddington luminosity of a white-dwarf are calculated as functions of the mass. In the bottom panel, the mass-radius relationship of Pringle and Webbink (1975) is assumed, based on which the surface gravity and the temperatures at the Eddington luminosities are calculated. In the middle and top panels, the best-fit temperatures and luminosities of CAL87 determined using the LTE and NLTE models are indicated by thick lines. The steady nuclear burning zone of the SSS model by van den Heuvel et al. (1996) is shown in the top figure, as well as the range of the observed CAL87 luminosity assuming isotropic emission. See texts for further explanations.

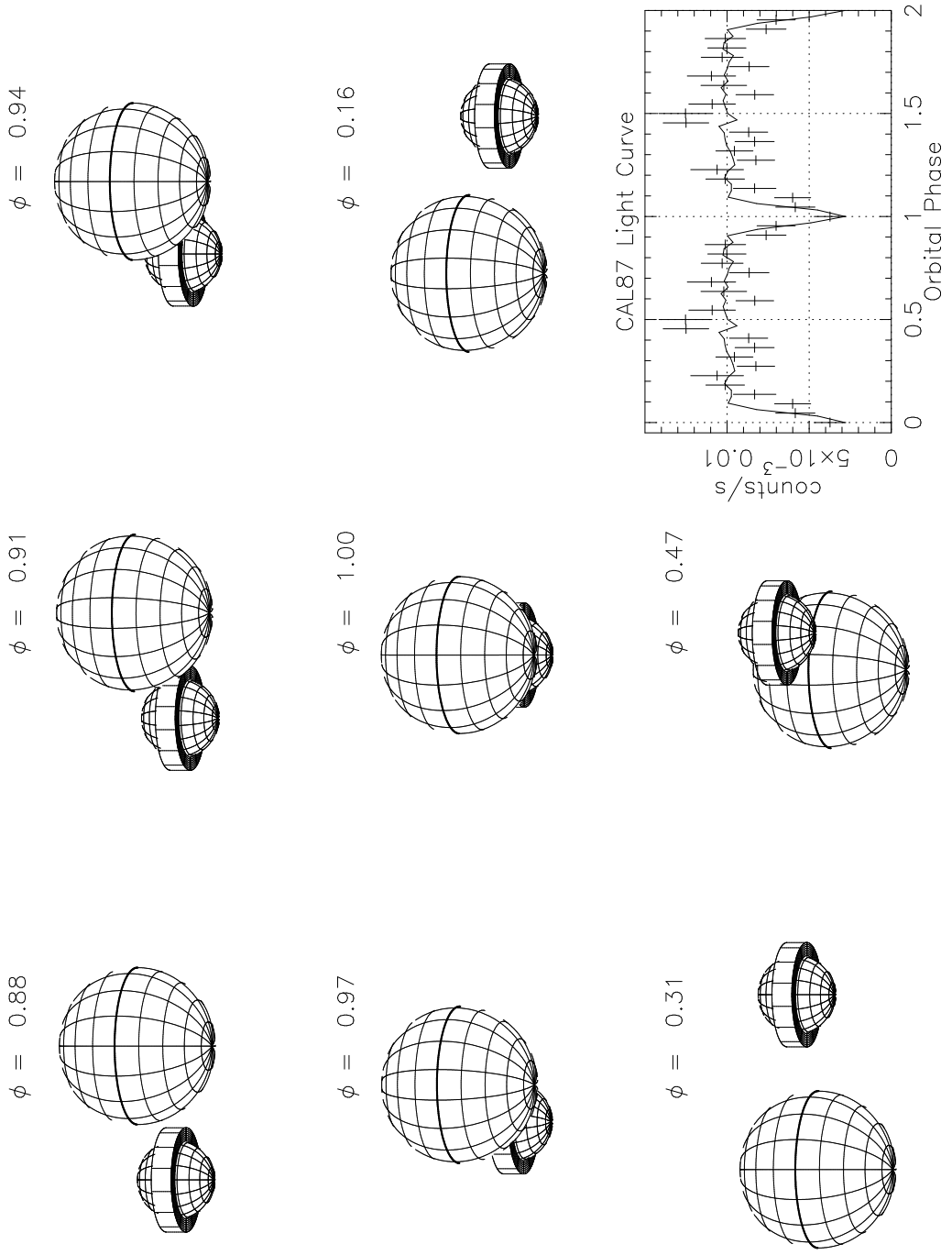

Fig. 14.— Simulation of the CAL87 X-ray orbital light curve with the Accretion Disk Corona (ADC) model. The smaller sphere represents the X-ray emitting ADC, and the surrounding "band" is the accretion disk to block the X-rays from the white dwarf and ADC. X-ray flux is assumed to be proportional to the projected ADC surface area which is not blocked by either companion star (filling its Roche lobe) or accretion disk. The accretion disk radius is assumed to be 0.8 times the white dwarf Roche lobe radius, and the ADC radius is 0.75 times the disk radius. Inclination angle is 73°. For other orbital parameters used, see texts.